

# A Two-Fold Patch Selection Approach for Improved 360-Degree Image Quality Assessment

Abderrezzaq Sendjasni, *Member, IEEE*, Seif-Eddine Benkabou, Mohamed-Chaker Larabi, *Senior Member, IEEE*

**Abstract**—This article presents a novel approach to improving the accuracy of 360-degree perceptual image quality assessment (IQA) through a two-fold patch selection process. Our methodology combines visual patch selection with embedding similarity-based refinement. The first stage focuses on selecting patches from 360-degree images using three distinct sampling methods to ensure comprehensive coverage of visual content for IQA. The second stage, which is the core of our approach, employs an embedding similarity-based selection process to filter and prioritize the most informative patches based on their embeddings similarity distances. This dual selection mechanism ensures that the training data is both relevant and informative, enhancing the model's learning efficiency. Extensive experiments and statistical analyses using three distance metrics across three benchmark datasets validate the effectiveness of our selection algorithm. The results highlight its potential to deliver robust and accurate 360-degree IQA, with performance gains of up to 4.5% in accuracy and monotonicity of quality score prediction, while using only 40% to 50% of the training patches. These improvements are consistent across various configurations and evaluation metrics, demonstrating the strength of the proposed method. The code for the selection process is available at: <https://github.com/sendjasni/patch-selection-360-image-quality>.

**Index Terms**—Image quality assessment, Convolutional Neural Networks, 360-degree images, Embedding similarity, and Learning optimization.

## I. INTRODUCTION

THE rapid advancement of virtual reality (VR), augmented reality (AR), and immersive multimedia technologies has significantly increased the demand for high-quality 360-degree images and videos [1], [2]. These formats offer users a more realistic and engaging experience by allowing them to explore their surroundings interactively. Ensuring the visual quality of 360-degree images is crucial for delivering a seamless user experience, which in turn drives the success of these technologies [1], [3]. However, evaluating the quality of 360-degree images poses unique challenges compared to traditional 2D images. Due to their spherical shape, these images are prone to complex distortions and uneven sampling, leading to variations in perceived quality across different regions. Furthermore, the immersive and interactive nature of applications using 360-degree content means that factors such as viewing conditions, user expectations, and visual exploration patterns also influence the perceived quality [4].

This work is partially funded by the Nouvelle-Aquitaine research council under projects SIMOREVA360 2018-1R50112 and PERCEIVE AAPR2020-2019-8498010.

This work has been submitted to IEEE Transactions for possible publication. Copyright may be transferred without notice, after which this version may no longer be accessible.

Given these challenges, it is crucial to gain a better understanding of the perceptual quality of 360-degree images and develop reliable methods to evaluate and enhance them. Deep learning has emerged as a promising solution to address the challenges of assessing the perceptual quality of 360-degree images. By using artificial neural networks, deep learning models can learn intricate patterns and accurately predict human perception of image quality. Recent progress in this field has led to the creation of various deep learning-based models for 360-degree image quality assessment (IQA) [5]–[11], which have demonstrated significant improvements in accuracy and efficiency compared to conventional quality metrics, such as the PSNR-based [12] and SSIM-based [13] approaches.

While deep learning-based models have made considerable strides in 360-degree perceptual IQA, challenges and opportunities for further improvement remain. A key limitation is their reliance on large, annotated datasets for training, which can be costly and time-intensive to produce, especially for specialized tasks like IQA [14], [15]. Moreover, the effectiveness of these models is highly dependent on the quality and diversity of the training data, often leading to suboptimal performance in real-world applications. Current methods frequently utilize selected viewports [10], [16]–[18] or patches [19]–[22] as samples to construct and enhance training datasets, with selection criteria based on task-specific factors such as cube-map projection [17], [23], saliency [18], and scan paths [8]. However, these criteria do not always guarantee the representativeness and reliability of the training data, which can hinder the model's generalization performance. Projection-based methods are prone to over-sampling, while saliency and scan-path-based approaches may introduce biases due to their dependence on data-driven models. Relying exclusively on such selected samples can limit the potential for improvement in training and generalization, ultimately affecting the performance and accuracy of deep learning models for 360-degree perceptual IQA. To overcome these challenges, exploring alternative selection methods and strategies is crucial to ensure more diverse, representative, and reliable training datasets.

In IQA, supervised learning is the most widely used approach, where models are trained to predict image quality based on labeled examples from the training dataset. These datasets typically include numerous samples from 360-degree images; however, not all samples contribute equally to the prediction task and may introduce noise. Therefore, effective sample selection is essential for improving prediction accuracy by focusing on the most informative samples [24]. By

retaining relevant training samples and eliminating redundant or irrelevant ones, we can reduce noise, optimize the training process, and enhance the performance of IQA models. From an IQA perspective, this ensures that only patches consistent with perceptual MOS are retained.

To drive further advancements in 360-degree perceptual IQA, this article introduces a novel two-fold patch selection method designed to improve both accuracy and robustness. The first stage involves selecting patches from 360-degree images using three distinct strategies: projection-based, latitude-based, and visual trajectory-based sampling. In the second stage, the selection is further refined based on the embedding similarity of the chosen patches, ensuring that only the most informative patches aligned with the learning objectives are retained, while redundant or irrelevant ones are discarded. Extensive experiments on benchmark datasets demonstrate the effectiveness of the proposed selection strategy, regardless of the sampling method employed. The key contributions of our work are summarized as follows:

- We propose a novel framework for adaptive patch selection to enhance the training and prediction performance of CNN-based 360-degree IQA models.
- We introduce an advanced embedding-based refinement process that improves the relevance of selected patches, maximizing their contribution to the learning task while minimizing redundancy.
- We validate the effectiveness of the proposed method through extensive experiments on benchmark datasets, showing significant improvements in accuracy and robustness across various configurations.

The remainder of the paper is organized as follows. Section II provides a review of relevant related work. Section III describes the proposed selection methodology. Section IV provides a comprehensive validation and discussion followed by conclusions and future works in Section V.

## II. RELATED WORK

This section provides a comprehensive review of the existing literature on 360-degree IQA, with a particular focus on deep learning-based models.

Early research in 360-degree image quality assessment concentrated on addressing the unique characteristics of spherical content. Initial approaches extended traditional 2D IQA models, such as PSNR and SSIM, by adapting them to handle non-uniform sampling during the conversion from spherical to planar projection [12], [13]. However, these methods had limited success, as they failed to account for perceptual aspects and how users interact with 360-degree images. This limitation led to the adoption of deep learning models, with multichannel networks emerging as a promising solution.

Multichannel CNNs operate by representing 360-degree images as multiple viewports [18], [25], [26], cubemap faces [6], [17], [27], [28], or patches [22], and then applying parallel pre-trained models to extract visual features. Although these approaches improved upon traditional methods, they still struggled with challenges related to content fidelity, user behavior modeling, and computational efficiency. As the number of

parallel models increased, so did the model's complexity, as evidenced by prior studies that utilized six [18], twenty [17], and even thirty-two [22] pre-trained networks. Additionally, the dependence on pre-trained CNNs made it difficult to adapt to diverse datasets and novel image content. The selection of the input representation and pre-trained model is also a crucial factor in determining the model's effectiveness [29].

As research in this field advanced, more sophisticated architectures and training strategies were developed to address these challenges. These included methods for better capturing user exploration behaviors, optimizing computational efficiency, and improving adaptability to a wider range of datasets.

Recent advances in 360-degree IQA involve leveraging advanced deep learning architectures, such as transformers [30], and integrating user behavior to enhance quality assessment accuracy [6], [8], [31]–[33]. The importance of incorporating factors like visual saliency and scan paths has been increasingly recognized, as these elements make IQA frameworks more aligned with perceptual assessments. While objective metrics provide valuable insights into image quality, they often fail to fully capture human perception. Consequently, recent studies have focused on integrating user-centric factors into 360-degree IQA methodologies to better match computational predictions with subjective evaluations.

To bridge the gap between user visual perception and objective model predictions, researchers have adopted techniques that incorporate human perceptual insights into the assessment process. For instance, visual trajectory analysis is used to identify the visual paths users follow when interacting with immersive content. By predicting the quality of 360-degree images based on areas users focus on, quality models can better align with human perception, resulting in more accurate computational predictions.

In this context, the TVFormer model introduced in [8] integrates head trajectories and transformers to predict 360-degree image quality. The model uses predicted head trajectories to sample relevant viewports for quality assessment, considering the interdependencies between viewports. TVFormer employs a hybrid approach where CNNs capture global features from the equirectangular projection (ERP), while transformers capture local spatio-temporal features from individual viewports. However, this method is limited by estimating only a single trajectory per image, which may not account for diverse user exploration patterns. To address this, the Assessor360 model [33] introduces a multi-sequence sampling strategy based on recursive probability sampling, allowing for multiple exploration trajectories based on different starting points. While this approach captures variability among users, it still heavily relies on the initial starting point, potentially limiting the exploration scope.

In contrast to scanpath approaches, the ST360IQ model [31] utilizes saliency to identify important regions in omnidirectional images, using a combination of ResNet-50 [34] and ViT [30] to encode and generate quality scores. Another hybrid model, combining ResNet-50 and ViT, is presented in [32], focusing on predicting the quality on CMP faces. These models have demonstrated superior performance compared to earlier works, such as MC360IQA [17] and VGCN [18], thanks to

the integration of advanced architectures and methodologies. However, despite improvements in preprocessing and content representation, the correlation among data in the constructed training set is often overlooked, leading to over-reliance on predefined sampling strategies, which may impair the model’s generalization capabilities.

To address this issue, more elaborate selection strategies can be employed to enhance deep learning models by retaining only the most relevant training samples. Adaptive selection methods can reduce the size of the original dataset to a manageable volume, minimizing computational resource requirements while removing noisy samples before training. This leads to more robust and scalable IQA solutions. Such techniques are widely used across various machine learning tasks [35], [36], yet their application to IQA, particularly in the 360-degree image context, remains largely unexplored.

In the following section, we present the proposed methodology for improving 360-degree IQA through a two-fold selection approach.

### III. THE PROPOSED METHODOLOGY

In this section, we introduce a novel methodology for improving learning-based 360-degree IQA, consisting of two important steps. The first step involves visual patch sampling from 360-degree images using three distinct sampling strategies. The second step refines the selection based on embedding similarities. By leveraging the rich feature representations extracted from these sampled patches, our approach focuses on selecting the most relevant samples for more accurate quality prediction. The following sections provide a detailed explanation of each step.

#### A. Notations

We start by introducing the notations used in this article. Sets are denoted by calligraphic letters (e.g.,  $\mathcal{D}$ ), matrices by bold uppercase letters (e.g.,  $\mathbf{X}$ ), vectors by bold lowercase letters (e.g.,  $\mathbf{a}$ ), and scalars by regular lowercase letters (e.g.,  $b$ ). Table I provides a summary of the relevant notations.

TABLE I  
SUMMARY OF SYMBOLS AND NOTATIONS

Symbol	Definition
$\mathcal{D}$	Collection of $m$ images $\mathbf{M}_i \in \mathbb{R}^{n_i \times d_i}$
$\mathcal{P}$	Collection of $n$ patches $\mathbf{p}_i \in \mathbb{R}^{x \times y \times 3}$
$\mathcal{E}$	Collection of $n$ embeddings $\mathbf{E}_i \in \mathbb{R}^{n_i \times d_i}$
$\mathbf{E}$	Embeddings representing $\mathbf{M}_i \in \mathbb{R}^{n_i \times d_i}$
$n_i$	Number of patches $\mathbf{p}_j$ in Image $\mathbf{M}_i$
$d_i$	Number of features in Image $\mathbf{M}_i$
$h$	Dimension of the low dimensional space
$\mathbf{W}_i \in \mathbb{R}^{d_i \times h}$	Transformation Matrix of Image $\mathbf{M}_i$
$\mathbf{R}_i \in \mathbb{R}^{h \times n_i}$	Residual Matrix of Image $\mathbf{M}_i$
$\mathbf{I}_k \in \mathbb{R}^{k,k}$	Identity Matrix
$\ \cdot\ _{2,1}; \ \cdot\ _F$	Matrix norms ( $\ell_{2,1}$ and Frobenius norms.)
$\ \mathbf{W}_i\ _{2,1}$	$\sum_{j=1}^{n_i} \ \mathbf{w}_i\ _2 = \sum_{i=1}^{d_i} \sqrt{\sum_{j=1}^h w_{ij}^2}$ .
$\ \mathbf{M}_i\ _F$	$\sqrt{\text{Tr}(\mathbf{M}_i^T \mathbf{M}_i)} = \sqrt{\sum_{j=1}^{n_i} \sum_{k=1}^{d_i}  p_{jk} ^2}$ .

#### B. Visual Patch Selection

Given the high resolution (4K+) and diverse content of 360-degree images, directly using entire images for quality assessment is inefficient [29]. This is particularly true in deep learning approaches, where visual content is heavily compressed into latent spaces. As a result, a sampling step is necessary to focus on key regions of interest, enhancing the precision of the quality assessment process. In this study, we explore three patch sampling methods, each representing a distinct approach: uniform sampling from the equirectangular projection (ERP), latitude and importance-based sampling on the sphere, and multi-visual trajectory-based sampling. Figure 1 provides an illustration of these sampling methods.

Therefore, we define a sampling method as:

$$\Psi_n^{\text{samp}} : \mathbf{M} \in \mathbb{R}^{x,y,3} \rightarrow \mathcal{P} \in \mathbb{R}^{n \times x \times y \times 3}, \quad (1)$$

where  $\mathbf{M}$  represents the input 360-degree image,  $n$  is the number of patches, and  $\mathcal{P}$  is the resulting set of patches. The term *samp* defines the used sampling method.

**Uniform sampling from ERP:** The first method involves uniform sampling from the ERP of 360-degree images. Patches are evenly distributed across the entire image, ensuring all regions are equally represented, as illustrated in Fig. 1 (a). This method serves as a baseline and provides a general overview of the image quality without focusing on specific regions. Non-overlapping patches of size  $128 \times 128$  pixels are sampled from each image  $\mathbf{M}$ . The set of patches sampled is represented as  $\mathcal{P}^{\text{ERP}}$  and can be obtained by:

$$\mathcal{P}^{\text{ERP}} = \Psi_n^{\text{ERP}}(\mathbf{M}), \quad (2)$$

where the location of each patch is obtained by:

$$u = u_{\min} + i \cdot \Delta u \cdot s, \quad v = v_{\min} + j \cdot \Delta v \cdot s, \quad (3)$$

with  $u_{\min}$  and  $v_{\min}$  the minimum coordinates in the ERP,  $\Delta u$  and  $\Delta v$  are the intervals between sampled patches in the horizontal and vertical directions, and  $s$  is the patch size (128 pixels). The indices  $i$  and  $j$  determine the patch’s position in the grid.

**Latitude and importance-based sampling:** Since the equatorial regions of 360-degree images tend to be more visually significant, this method gives more importance to these areas by sampling patches non-uniformly based on latitude from the spherical representation. The set  $\mathcal{P}^{\text{LAT}}$  is obtained by the sampling function:

$$\mathcal{P}^{\text{LAT}} = \Psi_n^{\text{LAT}}(\mathbf{M}). \quad (4)$$

This function starts from the equator and samples patches at decreasing intervals toward the poles, prioritizing equatorial regions. At the equator, patches are defined with an initial latitude  $\alpha_0$ . The sampling levels and coordinates are determined by:

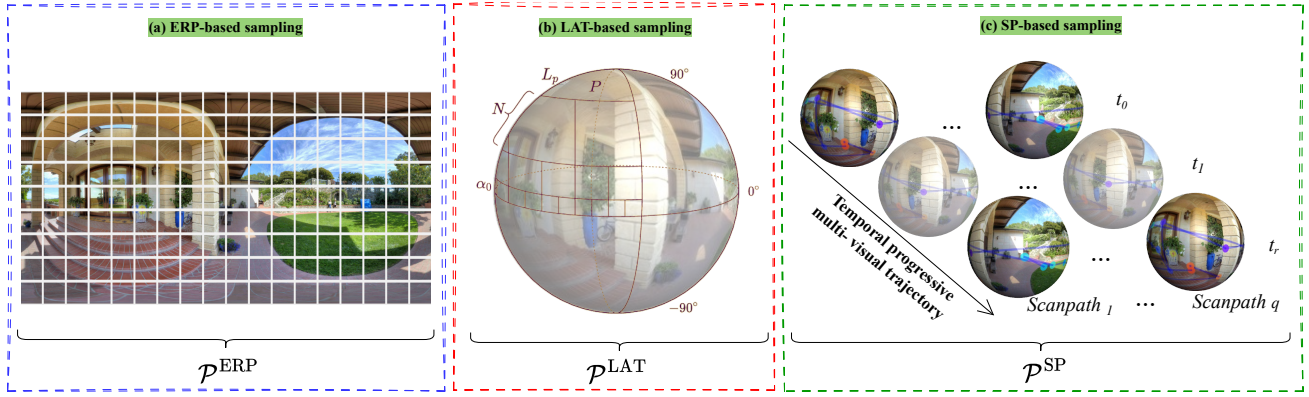


Fig. 1. Illustration of the sampling methods used in this study. Each method processes the input images and generates a set of patches  $\mathcal{P}$ .

$$\exists \alpha_0 > 0 : \frac{360}{\alpha_0} \in \mathbb{N}^+ \text{ and } \frac{360}{\alpha_0 \cdot 2^N} \in \mathbb{N}^+, \quad (5)$$

where  $N$  is the last sampling level before the polar region  $P$ . Patches in the next level are double the size in latitude and longitude, as illustrated in Fig. 1 (b). The number of sampling levels is determined by:

$$\exists N \geq 0 : (1 + \sum_{i=0}^N 2^i) \alpha_0 + L_P = 90 \text{ and } L_P < \alpha_N, \quad (6)$$

where  $L_P$  is the polar region latitude. The latitude and longitude coordinates of each patch are then determined by the following:

$$\theta = \theta_{min} + i \cdot \Delta\theta, \quad \phi = \phi_{min} + j \cdot \Delta\phi, \quad (7)$$

where  $\theta$  and  $\phi$  represent the latitude and longitude, respectively, of each patch.  $\theta_{min}$  and  $\phi_{min}$  are the minimum coordinates at each sampling level, and  $\Delta\theta$  and  $\Delta\phi$  are the angular intervals between patches in latitude and longitude, respectively. The indices  $i$  and  $j$  correspond to the patch's position in the grid at the respective latitude band.

As the sampling progresses toward the poles, patch sizes increase to ensure that the entire image is covered while ensuring a higher density of patches in the equatorial region, which is perceptually more significant. Finally, all patches, regardless of their original size, are resampled to match the size of the equatorial patches ( $128 \times 128$  pixels).

**Multi-visual trajectory-based sampling:** This method utilizes predicted scanpaths, representing multi-visual trajectories, to sample patches on the spherical surface. The human visual system (HVS) instinctively focuses on salient features in a visual scene, leading to eye fixations [37]. The content characteristics influence the progression of these visual trajectories, resulting in the formation of scanpaths. Each fixation point along the scanpath is considered a potential center for identifying patches.

To better reflect user behavior, it is crucial to account for the variability in how different users explore 360-degree content.

Since the final perceptual quality score of an image is often derived from multiple user assessments, which may focus on different regions, this variability is captured by predicting multiple scanpaths for each image as illustrated in Fig. 1 (c). To handle the complexity of 360-degree imagery and minimize distortions from projections like the ERP, we adopt a spherical representation for this sampling method. This method generates:

$$\mathcal{P}^{\text{SP}} = \Psi_n^{\text{SP}}(\mathbf{M}). \quad (8)$$

For each input image  $\mathbf{M} \in \mathbb{R}^2$ , a function is applied to project points from the Cartesian plane onto the spherical domain, preserving the spatial characteristics of the original image. A visual scanpath is then defined as a sequence of fixation points in the spherical domain. Thus, for each image  $m$ , we predict  $q$  scanpaths, denoted as  $\mathcal{S}m = \mathcal{S}p_i^1, \mathcal{S}p_i^2, \dots, \mathcal{S}p_i^q$ . The locations of potential patches are identified as  $\{f_{mj}^k\}_{j=1}^r$  corresponding to the temporal progression of the visual exploration  $\{t_i\}_{i=0}^r$ , where  $f_{mj}^k$  represents the  $j$ -th fixation point in the  $k$ -th predicted scanpath for image  $m$ . Each fixation point serves as the center of a patch, ensuring that the sampling is aligned with areas that are visually salient based on the predicted scanpaths.

For scanpath prediction, we use the ScanGAN360 model [38], a generative adversarial network (GAN)-based approach, that has shown strong performance in earlier studies [39]. ScanGAN360 leverages generative adversarial networks to predict scanpaths that closely emulate human gaze behavior, providing realistic fixation points for patch sampling in 360-degree images.

### C. Patch Encoding and Feature Representation

At this stage, visual details from each patch are encoded into a latent space, yielding informative and compressed feature representations via CNNs. For each sampling method, patches are fed into a CNN model that encodes their visual features into feature maps  $f_{\text{net}}(\mathcal{P}) \in \mathbb{R}^{x \times y \times 3}$ .

The primary goal of encoding these patches into a latent space is to transform the raw pixel data into a more meaningful and compact representation. This transformation facilitates the

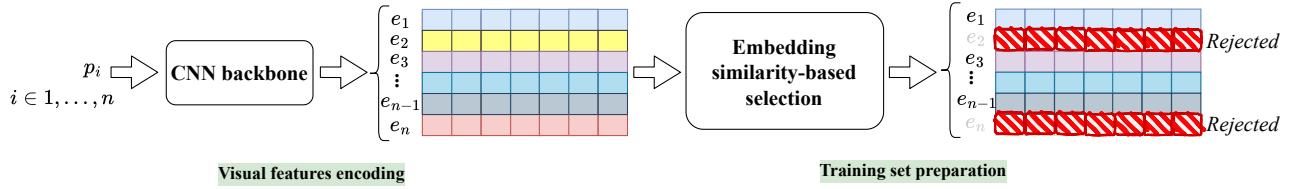


Fig. 2. Overview of the proposed embedding similarity-based selection framework. Visual patches  $\mathbf{p}_i$  are encoded into embeddings  $\mathbf{e}_i$ , and selected based on their similarity to other embeddings from the same image.

extraction of salient features, which are critical for various downstream tasks, such as IQA. By capturing essential visual characteristics while discarding irrelevant information, the embeddings allow for a more efficient content analysis.

To reduce dimensionality and focus on significant patterns, we apply global average pooling (GAP)  $g(\cdot)$  to the feature maps  $f_{\text{net}}(\mathcal{P})$ . This operation computes the average of each feature channel across the spatial dimensions, resulting in an embedding set  $\mathbf{E} \in \mathbb{R}^{n \times c}$ :

$$\mathbf{E} = g(f_{\text{net}}(\Psi_n^{\text{samp}}(M))). \quad (9)$$

This operation not only reduces the dimensionality but also emphasizes the most relevant features, which are crucial for understanding the perceptual quality of the patches. We utilize the ResNet-50 model [34] for feature encoding, which generates embeddings of size 2048 elements. The ResNet architecture is particularly effective for deep learning tasks due to its use of skip connections, enabling the network to learn residuals rather than direct mappings. This design mitigates the vanishing gradient problem often encountered in deep networks, allowing for improved performance in feature extraction. The resulting embeddings serve as a rich representation of the visual content, encapsulating essential characteristics such as color distribution, texture, and structural patterns.

After selecting patches using one of the sampling strategies described in Sec. III-B, we refine the selection process by analyzing the characteristics of the patch embeddings ( $\mathbf{E}$ ), within the learned feature space. While the initial sampling ensures that visually significant regions are included, it is crucial to analyze to further examine the inter-relationships among these patches at a more abstract level. To this end, we apply an embedding similarity-based selection that prioritizes patches not only for their visual importance but also for their structural distinctiveness, capturing complex patterns that significantly impact perceptual quality. The following section provides a detailed explanation of the embedding-based selection algorithm and its underlying criteria.

#### D. Embedding Similarity-Based Selection

The objective of this component of our framework is to identify the most relevant embeddings and eliminate those that do not provide valuable information for the learning task (e.g., supervised classification). To achieve this, we leverage the concept of similarity preservation, commonly applied for

feature selection in tabular data [40], and combine it with residual analysis to perform patch selection.

Let  $\mathcal{D} = \{\mathbf{M}_1, \dots, \mathbf{M}_m\}$  be a collection of  $m$  images  $\mathbf{M}_i$  and each image  $\mathbf{M}_i \in \mathbb{R}^{n_i \times d_i}$  is represented by  $n_i$  patches  $\mathbf{p}_j \in \mathbb{R}^{d_i}$  and viewed as  $n_i \times d_i$  matrix.  $\mathcal{E} = \{\mathbf{E}_1, \dots, \mathbf{E}_m\}$  is representing the embeddings of  $\mathcal{D}$  obtained by Eq. 9.

Selecting the best features subset according to the similarity preserving technique consists at fitting a transformation matrix  $\mathbf{W}_i$  that maps the high-dimensional  $\mathbf{E}_i$  to reduced-space  $\mathbf{E}_i \mathbf{W}_i$  while preserving the similarity structure of embeddings of  $\mathbf{E}_i$  and  $\mathbf{E}_i \mathbf{W}_i$ . This problem can be formulated as minimizing the difference between the similarity matrix of the patches' embeddings in the original space and the other one in the lower space:

$$\min_{\mathbf{W}_i} \| (\mathbf{E}_i \mathbf{W}_i)(\mathbf{E}_i \mathbf{W}_i)^\top - \mathbf{S}_i \|_F^2 + \alpha \| \mathbf{W}_i \|_{2,1}, \quad (10)$$

where :

- $\mathbf{S}_i$  represents the similarity matrix computed in the embedding space  $\mathbf{E}_i$ . We utilize three distance metrics to measure similarity: Euclidean (EUC), Manhattan (MAN), and Mahalanobis (MAH) [41]. These metrics are selected to capture different dimensions of similarity [42]: Euclidean distance measures the straight-line distance, offering a simple and efficient calculation; Manhattan distance sums the absolute differences, providing robustness against outliers; and Mahalanobis distance accounts for correlations between features, enabling a more accurate similarity measure, especially when dealing with varying scales and distributions.
- $\mathbf{W}_i \in \mathbb{R}^{d_i \times h}$  represents the transformation matrix, where  $h$  ( $(h \ll d_i)$ ) denotes the dimensionality of the lower space  $\mathbf{E}_i \mathbf{W}_i$ .
- $\alpha \| \mathbf{W}_i \|_{2,1}$  is the regularization term, promoting sparsity of the coefficients  $\mathbf{W}_i$  which is crucial for effective feature selection.

However, minimizing the problem (10) directly is NP-hard and cannot be solved efficiently. It can be shown that, given a similarity matrix  $\mathbf{S}$ , an optimal solution of :

$$\min_{\mathbf{X} \in \mathbb{R}^{n \times h}} \| \mathbf{X} \mathbf{X}^\top - \mathbf{S} \|_F^2, \quad (11)$$

is

$$\mathbf{X}^* = \Lambda_{n \times h} \sqrt{\mathbf{D}_h}, \quad (12)$$

where  $\Lambda(\cdot, i)$  represents the  $h$  eigenvectors of  $\mathbf{S}$  corresponding to the  $h$  largest eigenvalues, which form the diagonal elements

of  $\mathbf{D}_h$ . Consequently, the problem (10) can be reformulated as follows :

$$\min_{\mathbf{W}_i} \|\mathbf{E}_i \mathbf{W}_i - \mathbf{Z}_i\|_F^2 + \alpha \|\mathbf{W}_i\|_{2,1}, \quad (13)$$

when  $\mathbf{Z}_i \in \mathbb{R}^{n_i \times h}$  is the eigen-decomposition of the similarity matrix ( $\mathbf{S}_i = \mathbf{Z}_i \mathbf{Z}_i^\top$ ).

To refine embeddings through feature selection, we incorporate residual analysis into problem (13). The underlying assumption is that after the transformation and projection into the reduced space, the similarity structure of the relevant embeddings will be preserved, whereas that of the irrelevant embeddings will not. Based on this assumption, we introduce a new variable,  $\mathbf{R}_i$ , into our objective function to weight the patches  $\mathbf{p}_j$  for the image  $\mathbf{E}_i$ . The matrix  $\mathbf{R}_i$ , which acts as a residual matrix, is defined as follows:

$$\mathbf{R}_i = (\mathbf{E}_i \mathbf{W}_i)^\top - \mathbf{Z}_i^\top - \Theta, \quad (14)$$

where  $\Theta$  is a random matrix assumed to follow a multi-dimensional normal distribution [43]. The residual matrix is used to identify irrelevant patches whose similarity could not be preserved. Each column of  $\mathbf{R}_i$  corresponds to a patch  $\mathbf{p}_j$  in  $\mathbf{E}_i$ . A large  $\ell_2$ -norm of  $\mathbf{R}_i(:, j)$  indicates that the patch  $\mathbf{p}_j$  is likely irrelevant. Based on this, we propose to perform patch selection by solving the following optimization problem:

$$\min_{\mathbf{W}_i, \mathbf{R}_i} \|\mathbf{E}_i \mathbf{W}_i - \mathbf{Z}_i - \mathbf{R}_i^\top\|_F^2 + \alpha \|\mathbf{W}_i\|_{2,1} + \beta \|\mathbf{R}_i\|_{2,1}, \quad (15)$$

where  $\beta$  is the regularization hyper-parameter, used to control the number of patches to be selected through  $\mathbf{R}_i$ .

### E. Optimization

Since the objective function in (15) is not convex with respect to  $\mathbf{W}_i$  and  $\mathbf{R}_i$  simultaneously, we adopt an alternating optimization approach over them. Additionally, this problem it is not smooth due to the use of  $\ell_{2,1}$ -norm on the regularization terms. To smooth it, we relax  $\|\mathbf{W}_i\|_{2,1}$  by  $Tr(\mathbf{W}_i \mathbf{D}_{\mathbf{W}_i} \mathbf{W}_i)$  and  $\|\mathbf{R}_i\|_{2,1}$  by  $Tr(\mathbf{R}_i \mathbf{D}_{\mathbf{R}_i} \mathbf{R}_i)$  as in [44], where  $\mathbf{D}_{\mathbf{W}_i}$  and  $\mathbf{D}_{\mathbf{R}_i}$  are a diagonal matrices with the  $i^{th}$  diagonal element equal to  $\frac{1}{2\|\mathbf{W}_i(:, i)\|_2}$  and  $\frac{1}{2\|\mathbf{R}_i(:, i)\|_2}$ , respectively. Finally, we solve the original problem, by addressing these two reduced and relaxed problems :

#### Update the Transformation Matrix $\mathbf{W}_i$ :

When  $\mathbf{R}_i$  is fixed, the objective function in (15) is convex w.r.t  $\mathbf{W}_i$ . Therefore, we consider the Lagrangian function of (15) :

$$\mathcal{L}_{\mathbf{W}_i} = Tr(\mathbf{W}_i^\top \mathbf{E}_i^\top \mathbf{E}_i \mathbf{W}_i - 2\mathbf{W}_i^\top \mathbf{E}_i^\top (\mathbf{R}_i^\top + \mathbf{Z}_i)) + \alpha \|\mathbf{W}_i\|_{2,1}. \quad (16)$$

Then, we compute the derivative of  $\mathcal{L}_{\mathbf{W}_i}$  w.r.t  $\mathbf{W}_i$  :

$$\frac{\partial \mathcal{L}_{\mathbf{W}_i}}{\partial \mathbf{W}_i} = 2\mathbf{E}_i^\top \mathbf{E}_i \mathbf{W}_i + \frac{\alpha \mathbf{W}_i}{\|\mathbf{W}_i(:, i)\|_2} - 2\mathbf{E}_i^\top (\mathbf{R}_i^\top + \mathbf{Z}_i), \quad (17)$$

and we set the equation (17) to zero to have the closed form

of  $\mathbf{W}_i$ :

$$\mathbf{W}_i = \left( \mathbf{E}_i^\top \mathbf{E}_i + \frac{\alpha \mathbf{I}_{d_i}}{\|\mathbf{W}_i(:, i)\|_2} \right)^{-1} \mathbf{E}_i^\top (\mathbf{R}_i^\top + \mathbf{Z}_i). \quad (18)$$

#### Update the Residual Matrix $\mathbf{R}_i$ :

Similarly to the previous problem, when  $\mathbf{W}_i$  is fixed, the objective function in (15) becomes convex w.r.t  $\mathbf{R}_i$ . Therefore, we consider the Lagrangian function of (15) :

$$\mathcal{L}_{\mathbf{R}_i} = Tr(\mathbf{R}_i^\top \mathbf{R}_i - 2\mathbf{R}_i^\top (\mathbf{E}_i \mathbf{W}_i - \mathbf{Z}_i)) + \beta \|\mathbf{R}_i\|_{2,1}. \quad (19)$$

Similarly, we compute the derivative of  $\mathcal{L}_{\mathbf{R}_i}$  w.r.t  $\mathbf{R}_i$  :

$$\frac{\partial \mathcal{L}_{\mathbf{R}_i}}{\partial \mathbf{R}_i} = \frac{\beta \mathbf{R}_i^\top}{\|\mathbf{R}_i(:, k)\|_2} + 2\mathbf{R}_i^\top - 2(\mathbf{E}_i \mathbf{W}_i - \mathbf{Z}_i), \quad (20)$$

and we set the equation (20) to zero to update  $\mathbf{R}_i$ :

$$\mathbf{R}_i = (\mathbf{E}_i \mathbf{W}_i - \mathbf{Z}_i)^\top \left( \frac{\|\mathbf{R}_i(:, k)\|_2 \mathbf{I}_{n_i}}{\|\mathbf{R}_i(:, k)\|_2 + \beta} \right)^\top. \quad (21)$$

---

### Algorithm 1 Embeddings selection

---

- 1: **input:**  $\mathbf{E}$ ,  $\alpha$ ,  $\beta$  and  $h$ .
  - 2: **output:** Top  $k$  relevant embeddings  $\mathbf{e}_j$  for  $\mathbf{E}$ .
  - 3: Compute the similarity matrix of  $\mathbf{S}$  embeddings  $\mathbf{E}$ .
  - 4: Get  $\mathbf{Z}$  such as  $\mathbf{S} = \mathbf{Z}\mathbf{Z}^\top$ , ( $\mathbf{Z} \in \mathbb{R}^{n \times h}$ ).
  - 5: Initialize the residual matrix  $\mathbf{R}$  by  $[\mathbf{0}]_{h \times n}$
  - 6: **while** convergence not reached **do**
  - 7:     Update  $\mathbf{W}$  and  $\mathbf{R}$  by (18) and (21) respectively.
  - 8: **end while**
  - 9: Rank the embedding  $\mathbf{e}_j$  of  $\mathbf{E}$  according to the  $\ell_2$ -norm of  $\mathbf{R}$  columns in ascending order ( $j = 1, \dots, n$ ).
- 

Based on equations (18) and (21), the post-processing steps for patch selection are outlined in Algorithm 1. Given a collection  $\mathbf{E}$ , of  $m$  embeddings, we begin by computing the matrix similarity  $\mathbf{S}$  for  $\mathbf{E}$  (line 3).  $\mathbf{S}$  is then eigen-decomposed to obtain the matrix  $\mathbf{Z}$ , which is used in the reformulated problem (line 4). The residual matrix  $\mathbf{R}$  is initialized by zero (line 6). We then iteratively update  $\mathbf{W}$  and  $\mathbf{R}$  until the objective in (15) converges. After convergence, the irrelevance score for each embedding  $\mathbf{e}_j$  in  $\mathbf{E}$  is computed based on its  $\ell_2$ -norm in the residual matrix  $\mathbf{R}$  (e.i.,  $\|\mathbf{R}_i(:, j)\|_2$ ). Finally, the embeddings are sorted by their irrelevance scores in ascending order, and the  $k$  most relevant patches are selected (line 9).

### F. Complexity Analysis

The computational complexity of the patch selection algorithm is presented in the following lemma :

**Lemma 1.** *The overall complexity of the algorithm is  $\mathcal{O}(h d_i t (d_i + n_i))$  where  $t$  represents the number of iterations.*

*Proof.* The time complexity of the algorithm mainly depends on the two operations involved in updating the variables  $\mathbf{W}_i$  and  $\mathbf{R}_i$  as described in (18) and (21), respectively. First,  $\mathbf{W}_i$  can be updated efficiently by solving the linear equation  $\left( \mathbf{E}_i^\top \mathbf{E}_i + \frac{\alpha \mathbf{I}_{d_i}}{\|\mathbf{W}_i(:, i)\|_2} \right) \mathbf{W}_i = \mathbf{E}_i^\top (\mathbf{R}_i^\top + \mathbf{Z}_i)$ , which

needs  $\mathcal{O}(h d_i^2)$ . Note that the expression  $\left(\mathbf{E}_i^\top \mathbf{E}_i + \frac{\alpha \mathbf{I}_{d_i}}{\|\mathbf{W}_i^{(k,:)}\|_2}\right)$  requires  $\mathcal{O}(d_i^2)$  while updating  $\mathbf{R}_i$  needs  $\mathcal{O}(n_i d_i h)$ .  $\square$

### G. Convergence Analysis

The alternating optimization proposed in Algorithm 1, to update  $\mathbf{W}_i$  and  $\mathbf{R}_i$  ensures that the objective function in (15) decreases with each iteration, guaranteeing the convergence of its value.

**Lemma 2.** *For two nonzero vectors,  $\mathbf{a}, \mathbf{b} \in \mathbb{R}^p$ , the following inequality holds:*

$$\|\mathbf{a}\|_2 - \frac{\|\mathbf{a}\|_2^2}{2\|\mathbf{b}\|_2} \leq \|\mathbf{b}\|_2 - \frac{\|\mathbf{b}\|_2^2}{2\|\mathbf{b}\|_2}. \quad (22)$$

**Theorem 1.** *The alternating optimization over  $\mathbf{W}_i$  and  $\mathbf{R}_i$  will decrease the objective function.*

*Proof.* By fixing  $\mathbf{R}_i^h$ , the  $\mathbf{W}_i^{h+1}$  is the solution of the following problem:

$$\min_{\mathbf{W}_i} \Phi(\mathbf{W}_i) = \|\mathbf{E}_i \mathbf{W}_i - \mathbf{Z}_i - \mathbf{R}_i^\top\|_F^2 + \alpha \|\mathbf{W}_i\|_{2,1}. \quad (23)$$

Furthermore, by approximating the  $\ell_{2,1}$ -norm of  $\mathbf{W}_i$  by  $Tr(\mathbf{W}_i^{h+1} \mathbf{D}_w \mathbf{W}_i^{h+1})$ , this inequality holds:

$$\begin{aligned} \|\mathbf{E}_i \mathbf{W}_i^{h+1} - \mathbf{Z}_i - \mathbf{R}_i^\top\|_F^2 + \alpha Tr(\mathbf{W}_i^{h+1} \mathbf{D}_w \mathbf{W}_i^{h+1}) \\ \leq \\ \|\mathbf{E}_i \mathbf{W}_i^h - \mathbf{Z}_i - \mathbf{R}_i^\top\|_F^2 + \alpha Tr(\mathbf{W}_i^h \mathbf{D}_w \mathbf{W}_i^h), \end{aligned} \quad (24)$$

and is equivalent to:

$$\begin{aligned} \|\mathbf{E}_i \mathbf{W}_i^{h+1} - \mathbf{Z}_i - \mathbf{R}_i^\top\|_F^2 + \alpha \|\mathbf{W}_i^{h+1}\|_{2,1} \\ - \alpha \left( \|\mathbf{W}_i^{h+1}\|_{2,1} - \sum_j \frac{\|\mathbf{W}_i^{h+1}\|_2^2(j,:)}{2\|\mathbf{W}_i^h\|_2(j,:)} \right) \\ \leq \|\mathbf{E}_i \mathbf{W}_i^h - \mathbf{Z}_i - \mathbf{R}_i^\top\|_F^2 + \alpha \|\mathbf{W}_i^h\|_{2,1} \\ - \alpha \left( \|\mathbf{W}_i^h\|_{2,1} - \sum_j \frac{\|\mathbf{W}_i^h\|_2^2(j,:)}{2\|\mathbf{W}_i^h\|_2(j,:)} \right). \end{aligned} \quad (25)$$

By integrating the inequality from the Lemma 1 in (25), we have:

$$\begin{aligned} \|\mathbf{E}_i \mathbf{W}_i^{h+1} - \mathbf{Z}_i - \mathbf{R}_i^\top\|_F^2 + \alpha \|\mathbf{W}_i^{h+1}\|_{2,1} \\ \leq \\ \|\mathbf{E}_i \mathbf{W}_i^h - \mathbf{Z}_i - \mathbf{R}_i^\top\|_F^2 + \alpha \|\mathbf{W}_i^h\|_{2,1}, \end{aligned} \quad (26)$$

which implies that:

$$\Phi(\mathbf{W}_i^{h+1}, \mathbf{R}_i^h) \leq \Phi(\mathbf{W}_i^h, \mathbf{R}_i^h). \quad (27)$$

Then, using  $\mathbf{W}_i^{h+1}$  and according to (21), we proceed to update  $\mathbf{R}_i^h$ , resulting in  $\mathbf{R}_i^{h+1}$ , which is the solution to the following optimization problem:

$$\min_{\mathbf{R}_i} \Phi(\mathbf{R}_i) = \|\mathbf{E}_i \mathbf{W}_i - \mathbf{Z}_i - \mathbf{R}_i^\top\|_F^2 + \alpha \|\mathbf{R}_i\|_{2,1}. \quad (28)$$

Similarly, we can prove that:

$$\Phi(\mathbf{W}_i^{h+1}, \mathbf{R}_i^{h+1}) \leq \Phi(\mathbf{W}_i^{h+1}, \mathbf{R}_i^h).$$

First, by approximating the  $\ell_{2,1}$ -norm of  $\mathbf{R}_i$  by  $Tr(\mathbf{R}_i^{h+1} \mathbf{D}_r \mathbf{R}_i^{h+1})$ , this inequality holds:

$$\begin{aligned} \|\mathbf{E}_i \mathbf{W}_i^{h+1} - \mathbf{Z}_i - \mathbf{R}_i^\top\|_F^2 + \beta Tr(\mathbf{R}_i^{h+1} \mathbf{D}_r \mathbf{R}_i^{h+1}) \\ \leq \\ \|\mathbf{E}_i \mathbf{W}_i^h - \mathbf{Z}_i - \mathbf{R}_i^\top\|_F^2 + \beta Tr(\mathbf{R}_i^h \mathbf{D}_r \mathbf{R}_i^h), \end{aligned} \quad (29)$$

and is equivalent to:

$$\begin{aligned} \|\mathbf{E}_i \mathbf{W}_i^{h+1} - \mathbf{Z}_i - \mathbf{R}_i^\top\|_F^2 + \beta \|\mathbf{R}_i^{h+1}\|_{2,1} \\ - \beta \left( \|\mathbf{R}_i^{h+1}\|_{2,1} - \sum_j \frac{\|\mathbf{R}_i^{h+1}\|_2^2(j,:)}{2\|\mathbf{R}_i^h\|_2(j,:)} \right) \\ \leq \|\mathbf{E}_i \mathbf{W}_i^h - \mathbf{Z}_i - \mathbf{R}_i^\top\|_F^2 + \beta \|\mathbf{W}_i^h\|_{2,1} \\ - \beta \left( \|\mathbf{R}_i^h\|_{2,1} - \sum_j \frac{\|\mathbf{R}_i^h\|_2^2(j,:)}{2\|\mathbf{R}_i^h\|_2(j,:)} \right). \end{aligned} \quad (30)$$

By integrating the inequality from the Lemma 1 in (30), we obtain:

$$\begin{aligned} \|\mathbf{E}_i \mathbf{W}_i^{h+1} - \mathbf{Z}_i - \mathbf{R}_i^\top\|_F^2 + \beta \|\mathbf{R}_i^{h+1}\|_{2,1} \\ \leq \\ \|\mathbf{E}_i \mathbf{W}_i^h - \mathbf{Z}_i - \mathbf{R}_i^\top\|_F^2 + \beta \|\mathbf{R}_i^h\|_{2,1}, \end{aligned} \quad (31)$$

implying that:

$$\Phi(\mathbf{W}_i^{h+1}, \mathbf{R}_i^h) \leq \Phi(\mathbf{W}_i^h, \mathbf{R}_i^h). \quad (32)$$

Finally, by combining the two inequalities (27) and (32), we derive the following inequality:

$$\Phi(\mathbf{W}_i^{h+1}, \mathbf{R}_i^{h+1}) \leq \Phi(\mathbf{W}_i^{h+1}, \mathbf{R}_i^h) \leq \Phi(\mathbf{W}_i^h, \mathbf{R}_i^h). \quad (33)$$

This indicates that the algorithm reduces the objective function at each iteration, progressively minimizing the error. As a result, the algorithm is guaranteed to converge to a solution.  $\square$

By leveraging the embedding similarity-based selection process, we effectively reduce the number of patches required for accurate quality prediction. This selective approach enables us to focus on the embeddings of patches have the most significant impact on perceived quality. In the subsequent step, these selected embeddings are used for quality estimation through a regression model. We employ a regression model, which learns the relationship between the selected embeddings and the Mean Opinion Score (MOS). The details of this process are provided in the following section.

### H. Quality Regression

For quality estimation, we employ a multi-layer perceptron (MLP) that utilizes the retained patch embeddings as input features to predict a quality score. The MLP is defined by the function  $\text{mlp}(\mathbf{e}_i)$ , where  $\mathbf{e}_i \in \mathbf{E}^*$  represents the embedding of the  $i$ -th patch, and  $\mathbf{E}^*$  the set of selected embeddings. The output of the MLP is the predicted mean opinion score (MOS), denoted as  $\text{pmos}$ .

The architecture of the MLP consists of an input layer that receives the patch embeddings, a hidden layer that performs nonlinear transformations, and an output layer that produces

the final quality score. The structure of the MLP is illustrated in Fig. 3. Specifically, the MLP can be represented as:

$$pmos = f(\mathbf{e}_i; \vartheta), \quad (34)$$

where  $f(\cdot; \vartheta)$  denotes the mapping function of the MLP, and  $\vartheta$  represents the parameters of the network, including weights and biases.

The MLP is trained to minimize the mean squared error (MSE) loss between the predicted quality score  $pmos$  and the ground truth MOS, which reflects the subjective quality assessments provided by human observers. The MSE loss function is defined as:

$$\mathcal{L}_{MSE}(mos, pmos) = \frac{1}{b} \sum_{i=1}^b (mos_i - pmos_i)^2, \quad (35)$$

where  $b$  is the number of samples in the mini-batch,  $mos_i$  is the ground truth score for the  $i$ -th patch, and  $pmos_i$  is the predicted score for the same patch.

By leveraging the retained embeddings through the selection algorithm, described in Sec. III-D, the MLP effectively captures the complex relationships between visual features and perceived quality, enabling robust quality regression for 360-degree images.

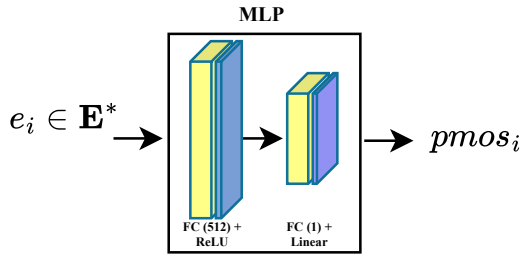


Fig. 3. The MLP used for quality score regression. It consists of two fully connected layers: the first with 512 neurons and ReLU activation, and the second with a single neuron and a linear activation to output the predicted score  $pmos$ .

Given that this study adopts a patch-based training approach, where the model is trained solely on individual patches extracted from the input images without access to the entire 360-degree image, a score aggregation is necessary. The model predicts  $n$  quality scores, one for each of the  $n$  sampled patches from a 360-degree image. To derive an overall quality score, these individual patch scores must be combined into a single value. For this purpose, we employ a weighted arithmetic mean, with the weights determined by the consistency of each score to the median of the set  $\mathcal{QL}$ , where  $\mathcal{QL} = \{pmos_1, pmos_2, \dots, pmos_n\}$ . The weights are as:

$$w_i = \frac{1}{|pmos_i - \text{median}(\mathcal{QL})|}, \quad (36)$$

and the final score is computed using the pooling function below:

$$pmos = \frac{\sum_{i=1}^n w_i pmos_i}{\sum_{i=1}^n w_i}. \quad (37)$$

This pooling strategy emphasizes scores closer to the median, aligning with subjective opinion aggregation principles, as recommended by ITU-R [45].

## IV. SIMULATIONS

### A. Experimental Protocol

**Computation Environment:** All experiments were conducted on a server equipped with an Intel Xeon Silver 4208 2.1GHz processor, 192GB of RAM, and an Nvidia Tesla V100S 32GB GPU.

**Benchmark Datasets:** The evaluation is performed using three well-established 360-degree IQA datasets: OIQA [17], CVIQ [17], and MVAQD [23]:

- **CVIQ:** Comprising 528 distorted 360-degree images, all at 4K resolution, this dataset was generated from 16 reference images, with distortions introduced through three compression techniques (JPEG, AVC, and HEVC) at 11 different levels.
- **OIQA:** including 320 distorted 360-degree images derived from 16 reference images, with four types of distortions (JPEG, JPEG 2000, Gaussian Noise (GN), and Gaussian Blur (GB)) applied at five levels.
- **MVAQD:** Containing 300 distorted images created from 15 pristine 360-degree images, this dataset applies five types of distortions (JPEG, JP2K, HEVC, BLUR, and White Noise (WN)) across four levels.

**Evaluation Criteria:** To assess quality prediction performance, we utilize two standard metrics: spearman’s rank-order correlation coefficient (SRCC) for monotonicity and pearson’s linear correlation coefficient (PLCC) for accuracy. A four-parameter regression model is applied prior to calculating these metrics. Additionally, statistical significance analysis is conducted to examine the impact of various parameters and their interactions on performance. Each dataset is randomly split into training (80%) and testing (20%) sets, based on pristine images. This process is repeated four times, and the median results are reported.

### B. Performance Analysis

To comprehensively assess the effectiveness of the proposed selection method, we analyze performance across selection rates ranging from 10% to 90%, comparing these results to the baseline scenario where no selection is applied (i.e., using 100% of the training samples). The performance, measured in terms of PLCC and SRCC, is presented as radar charts in Fig. 4 for OIQA, Fig. 6 for CVIQ, and Fig. 8 for MVAQD. These charts highlight the lowest selection rate that surpasses the performance of the baseline for each  $h$  value, where  $h$  represents the number of eigenvectors used in the embedding similarity-based selection. The values of  $h$  are drawn from the set  $\mathcal{H}^1$ , which covers a wide range to ensure a thorough evaluation across different scales.

<sup>1</sup> $\mathcal{H} = \{1, \dots, 10, 20, 61, 102, 204, 512, 1024, 2048\}$ , representing the number of eigenvectors derived from the similarity matrix, based on the patches’ embeddings obtained from ResNet-50.



If no improvement is observed, the plot line remains centered on the x-axis, indicating that the selection method did not enhance performance for that specific  $h$  value at any selection rate. The charts also demonstrate how various combinations of patch sampling methods, similarity distance metrics, selection rates, and  $h$  values compare to the baseline without embedding similarity-based selection. Certain combinations consistently outperform the baseline, suggesting reliable prediction performance.

1) **Performance analysis on OIQA:** As illustrated in Fig. 4, LAT-based sampling consistently emerges as the most effective method, showing improvements across all  $h$  values (representing eigenvectors) and similarity distance metrics. It achieves significant performance gains at a minimum selection rate of 40% for the Euclidean (EUC), Manhattan (MAN), and Mahalanobis (MAH) distance metrics. Notably, this indicates that the proposed selection method enhances quality prediction performance with only 40% of the training data, outperforming the baseline scenario where no selection is applied (100% of the data used).

In comparison, the ERP- and SP-based sampling methods yield improvements at minimum selection rates of 50% and 60%, respectively. Across all sampling methods and distance metrics, performance (in terms of PLCC and SRCC) tends to plateau once the selection rate reaches 40% to 50%. Beyond this threshold, further increases in the selection rate produce diminishing returns, suggesting that selective sampling effectively boosts performance up to a certain point, after which the benefits level off.

In the case of ERP-based sampling, SRCC improvements are more pronounced than those for PLCC, suggesting that projection-based sampling is particularly effective at preserving the rank order of predictions. This makes it a robust choice in scenarios where maintaining ranking consistency is more critical than achieving perfect linear correlation.

Regarding the optimal number of eigenvectors ( $h$ ) for effective selection, we observe that performance gains tend to saturate as  $h$  increases. This implies that using a smaller number of eigenvectors is sufficient for enhancing performance, while increasing  $h$  beyond a certain point adds little benefit.

To further evaluate the effects of sampling methods (ERP, SP, LAT), distance metrics (Euclidean, Manhattan, Mahalanobis), and the number of eigenvectors, we conducted an analysis of variance (ANOVA) with interaction terms. This allowed us to assess not only the main effects of each factor but also their potential interactions. By incorporating interaction terms in the ANOVA model, we were able to identify whether the influence of one factor depended on the others.

The heatmaps in Fig. 5 depict the p-values from the ANOVA analysis, highlighting the statistical significance of various parameters on PLCC and SRCC performance. The selection rate (Rate) consistently emerges as the most significant factor affecting performance for both metrics, exhibiting a strong effect. In contrast, the similarity distance metric (Dis.) and the number of eigenvectors ( $h$ ) show higher p-values, indicating a weaker or non-significant impact. This trend holds across all three sampling methods (ERP, LAT, SP), confirming the robustness of the embedding similarity-based selection approach

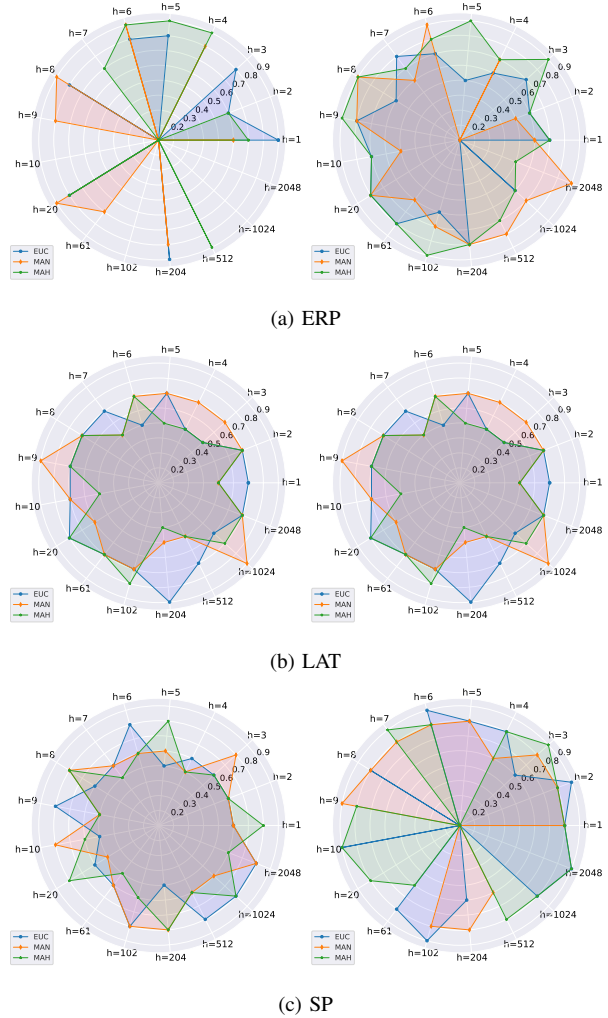


Fig. 4. Radar chart illustrating PLCC (first column) and SRCC (second column) across various  $h$  values and similarity distance metrics on the OIQA dataset. The x-axis represents the selection rates. The charts highlight the lowest selection rate that performed better than the baseline for each  $h$  value.

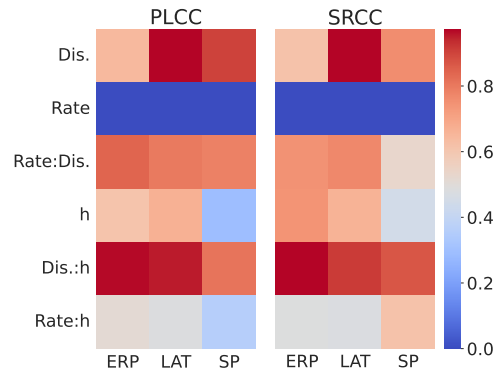


Fig. 5. Statistical significance of considered parameters and their interactions on PLCC and SRCC for the OIQA dataset. The heatmaps illustrate the p-values for (Dis.: similarity distance metrics, Rate: selection rate, and  $h$ : number of eigenvectors) and their interactions across three sampling methods (ERP, LAT, and SP).

regardless of the distance metric used. Additionally, the high p-values for the eigenvector count ( $h$ ) suggest that increasing the number of eigenvectors beyond a certain point has minimal effect on performance, underscoring the importance of identifying an optimal range for  $h$  to avoid unnecessary complexity.

2) **Performance analysis on CVIQ:** The performance on the CVIQ dataset exhibited a contrasting pattern compared to OIQA. Among the sampling strategies, ERP-based sampling proved to be particularly effective, delivering consistent improvements across all  $h$  values and similarity distance metrics. Remarkably, with a selection rate as low as 30%, the prediction accuracy surpassed that achieved with the entire training dataset. This underscores the efficiency of the proposed selection method in reducing the amount of data required for accurate predictions. Additionally, ERP-based sampling effectively handles geometrically distorted regions, such as the polar areas. By applying embedding-similarity-based selection, the generated samples are further refined, as evidenced by the significant performance improvements shown in Fig. 6.

LAT-based sampling, however, displayed considerable variability in performance across different  $h$  values and selection rates, indicating greater sensitivity to these factors. Similarly, SP-based sampling demonstrated a trend of performance improvement with increasing selection rates, though the gains were less pronounced at lower rates. Both LAT and SP sampling methods appear more context-dependent, as their effectiveness varied more noticeably with changes in  $h$  values and similarity metrics compared to ERP-based sampling.

In terms of accuracy, as measured by PLCC and SRCC, several key trends emerge. As  $h$  increases, PLCC values tend to stabilize, showing less variability. For instance, SP-based sampling with Mahalanobis distance starts with lower PLCC values at  $h = 1$ , but performance improves significantly as  $h$  increases, peaking around  $h = 8$  and plateauing thereafter. This pattern is consistent across all similarity metrics, indicating that higher  $h$  values contribute to more consistent and accurate predictions. Notably, the Mahalanobis distance consistently outperforms Manhattan and Euclidean distances, especially for intermediate  $h$  values (e.g.,  $h = 4$  to  $h = 10$ ). For optimal performance, an  $h$  range between 5 and 10 strikes a balance, offering minimal variability and robust performance across different distance metrics and sampling methods. This ensures both consistency and reliability in prediction accuracy.

The statistical analysis for the CVIQ dataset confirms that the selection rate (Rate) is the most influential factor affecting both PLCC and SRCC performance, as shown in Fig. 7. In contrast, the similarity distance metric (Dis.) and the number of eigenvectors ( $h$ ) exhibit minimal impact, with higher p-values indicating weaker or non-significant effects. This finding is consistent across all sampling methods (ERP, LAT, and SP), reinforcing the conclusion that optimizing the selection rate is key to improving performance, while other parameters play a relatively minor role.

3) **Performance analysis on MVAQD:** As shown in Fig. 8, the SP-based sampling strategy consistently outperforms the others in terms of both PLCC and SRCC across all similarity distance metrics and eigenvector values, followed by ERP and

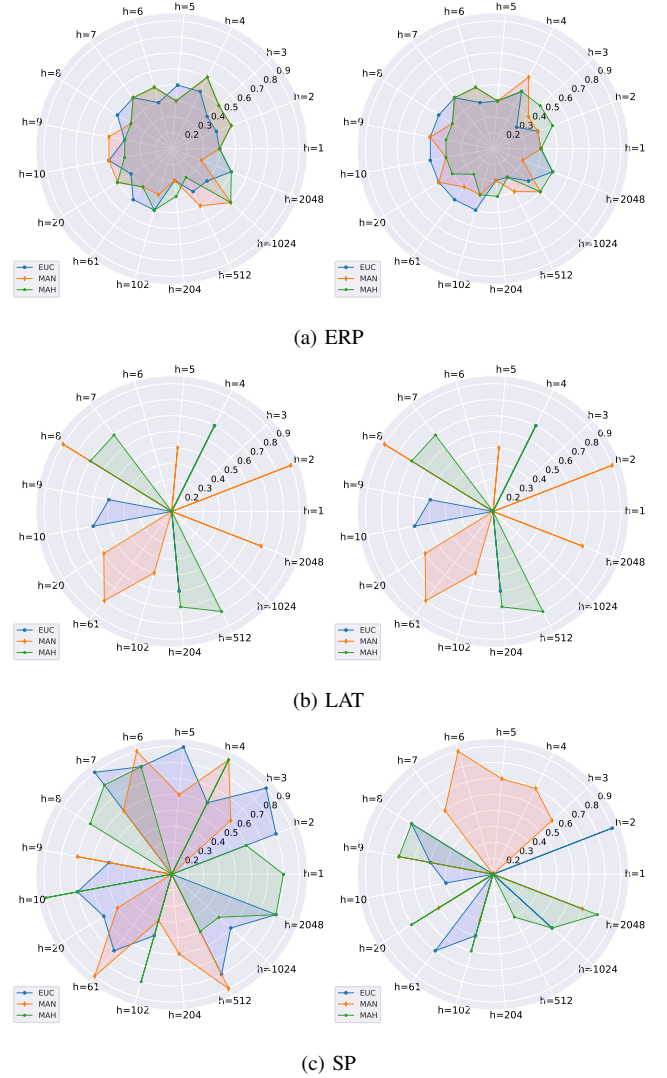


Fig. 6. Radar chart illustrating PLCC (first column) and SRCC (second column) across various  $h$  values and similarity distance metrics on the CVIQ dataset. The x-axis represents the selection rates. The charts highlight the lowest selection rate that performed better than the threshold for each  $h$  value.

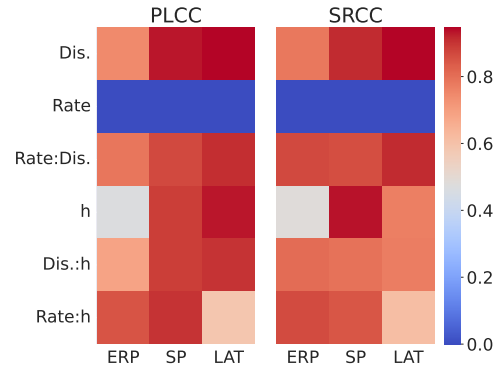


Fig. 7. Statistical significance of considered parameters and their interactions on PLCC and SRCC for the CVIQ dataset. The heatmaps illustrate the p-values for (Dis.: similarity distance metrics, Rate: selection rate, and  $h$ : number of eigenvectors) and their interactions across three sampling methods (ERP, LAT, and SP).

LAT. A selection rate of 40% to 50% which corresponds to using roughly half of the sampled patches proves effective in surpassing the performance of scenarios where no selection is applied. Beyond these selection rates, further improvements plateau, suggesting diminishing returns from additional training samples.

In terms of similarity distance metrics, the Euclidean distance performs consistently well across different sampling strategies. Its simplicity and efficiency make it a reliable choice for the selection process. On the other hand, the Manhattan and Mahalanobis distances show more variability in performance depending on the strategy used.

Regarding the number of eigenvectors ( $h$ ), SRCC exhibits less fluctuation compared to PLCC across different  $h$  values. This mirrors the trend observed in the OIQA dataset (see Fig. 4), where SRCC remains stable while PLCC varies more. This suggests that monotonicity, as measured by SRCC, is less sensitive to the number of eigenvectors used in the embedding similarity computation compared to accuracy, represented by PLCC. Interestingly, this behavior was not observed in the CVIQ dataset, which could be attributed to the heterogeneous nature of the distortions present in both the OIQA and MVAQD datasets, potentially influencing how eigenvectors affect performance metrics.

The statistical analysis for the MVAQD dataset, as presented in Fig. 9, aligns with the trends observed in the OIQA and CVIQ datasets. While some variability is observed in the interaction between the number of eigenvectors ( $h$ ) and selection rate, the Rate parameter consistently has the most significant impact on performance across all datasets. The low p-values associated with Rate in both PLCC and SRCC analyses underscore its critical role in determining the accuracy of the quality assessment model. This reinforces the conclusion that while other factors, such as eigenvectors and distance metrics, may have minor effects, the selection rate remains the most influential element in enhancing performance.

4) **Performance comparison:** To assess the performance gains from the proposed embedding similarity-based selection method, we calculated the percentage improvement in PLCC and SRCC compared to the baseline scenario without selection. Figure 10 summarizes the results across the OIQA, CVIQ, and MVAQD datasets, using different sampling methods (ERP, LAT, SP) and similarity distance metrics (EUC, MAN, MAH).

The proposed method demonstrates notable performance improvements across various configurations. For PLCC, the method achieves gains ranging from 1.18% to 3.68% on the OIQA dataset, with the highest improvement observed using the Mahalanobis (MAH) distance metric. In the CVIQ dataset, the ERP sampling method yields gains of up to 2.14%. For the MVAQD dataset, significant improvements are recorded, with gains ranging from 1.30% to 2.60%.

In terms of SRCC, the method results in improvements ranging from 0.30% to 3.29% for the OIQA dataset. The CVIQ dataset shows mixed results, with gains up to 4.08% using the MAH metric. For the MVAQD dataset, SRCC gains range from 2.94% to 4.5%, indicating strong performance across all metrics. Overall, the proposed method delivers

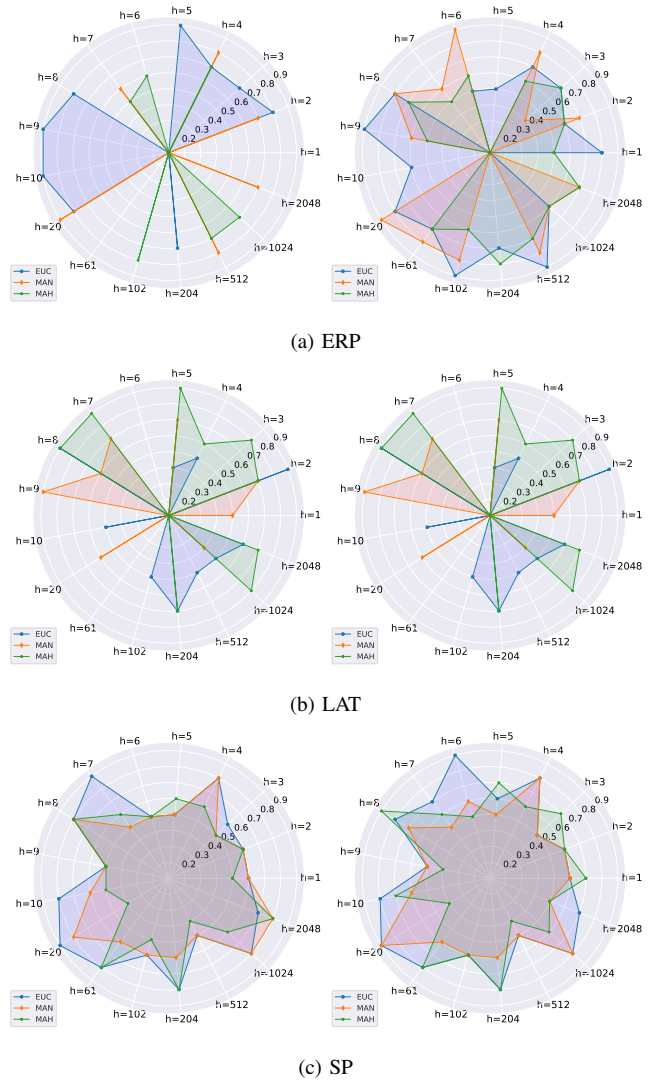


Fig. 8. Radar chart illustrating PLCC (first column) and SRCC (second column) across various  $h$  values and similarity distance metrics on the MVAQD dataset. The x-axis represents the selection rates. The charts highlight the lowest selection rate that performed better than the threshold for each  $h$  value.

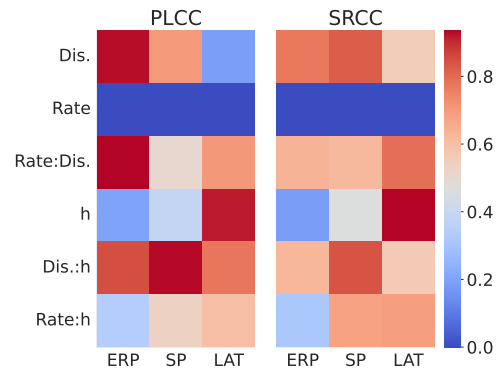


Fig. 9. Statistical significance of considered parameters and their interactions on PLCC and SRCC for the MVAQD dataset. The heatmaps illustrate the p-values for (Dis.: similarity distance metrics, Rate: selection rate, and h: number of eigenvectors) and their interactions across three sampling methods (ERP, LAT, and SP).

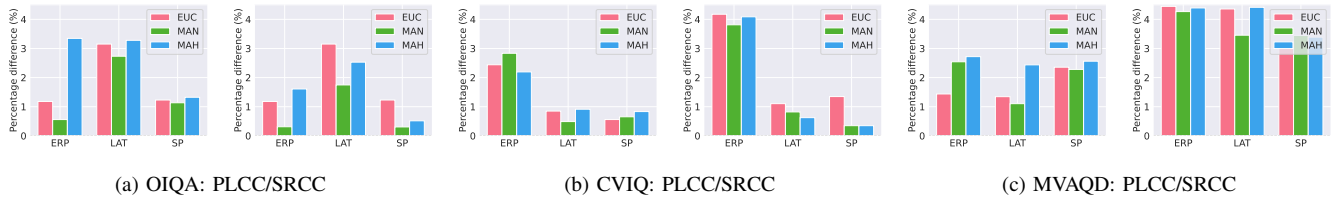


Fig. 10. Percentage performance gains of the proposed method in terms of PLCC and SRCC across datasets (OIQA, CVIQ, and MVAQD), sampling methods (ERP, LAT, SP), and similarity distance measures (EUC, MAN, MAH).

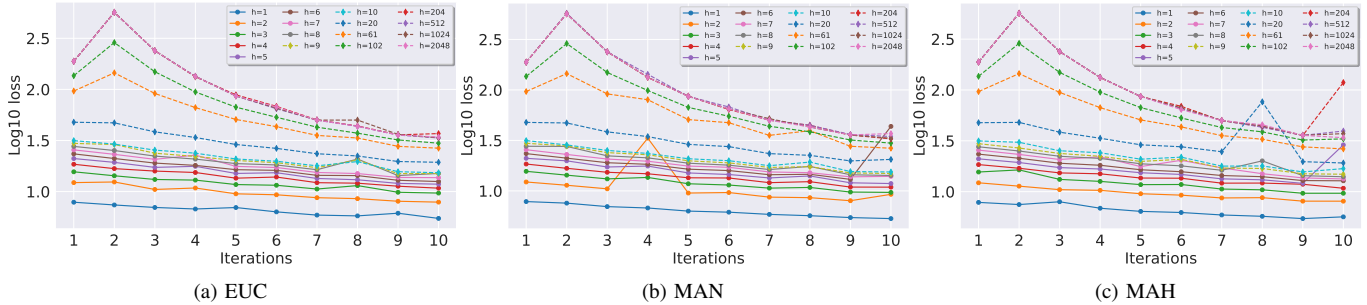


Fig. 11. Mean Log10 across all datasets and similarity distance metrics of the objective function’s loss for the selection algorithm over 10 iterations with varying numbers of eigenvectors ( $h$ ).

substantial performance gains across all datasets, regardless of the sampling method or distance metric used, although its effectiveness varies slightly depending on the specific dataset.

The differences in performance across distance metrics such as EUC, MAN, and MAH can be attributed to how each metric captures the similarity between embeddings. The MAH metric consistently shows higher gains, likely due to its ability to account for the covariance structure of the data, which makes it more sensitive to variations in the embedding space. This sensitivity enables it to better capture subtle differences in quality. While the EUC and MAN metrics are effective, they may not capture these nuances as precisely, resulting in comparatively lower gains.

However, it is important to note that the MAH metric is computationally more demanding than EUC and MAN. Calculating Mahalanobis distance involves inverting the covariance matrix, which can be resource-intensive, especially for high-dimensional data. In contrast, Euclidean and Manhattan distances are simpler and require fewer computational resources. Therefore, while the MAH metric offers better accuracy and performance gains, it does come at the cost of increased computational complexity.

### C. Convergence Evaluation of the Selection Algorithm

The loss function of the selection algorithm is defined as the Frobenius norm of the difference between  $\mathbf{XW}$  and  $\mathbf{R}^T + \mathbf{Z}$ , regularized by the  $L_{21}$  norms of  $\mathbf{W}$  and  $\mathbf{R}$ , as described in Sec. III-G. To support the proof of convergence described above, we analyze the loss behavior shown in Fig. 11. These curves demonstrate convergence across different numbers of eigenvectors ( $h$ ) and similarity distance metrics.

The loss behavior during optimization reflects the convergence characteristics of the algorithm. Initially, the loss is high due to the random initialization of  $\mathbf{W}$  and  $\mathbf{R}$ . As the algorithm progresses, the loss decreases as these matrices are updated

to better fit the data, minimizing the objective function. For higher values of  $h$ , the initial loss is greater because more eigenvectors contribute to the initial error. However, the algorithm converges after several iterations, indicating effective optimization. Conversely, lower values of  $h$  start with smaller initial losses, and convergence is achieved more quickly due to the simpler optimization problem.

This convergence behavior, as shown in the plots, demonstrates that regardless of the initial loss level (influenced by  $h$ ), the algorithm effectively reduces the loss and converges to a stable value. The consistent convergence across different eigenvector settings confirms the robustness and efficiency of the selection algorithm, validating its ability to minimize the objective function under various parameter configurations.

## V. CONCLUSION

In this study, we introduced a novel two-fold patch selection method designed to improve the accuracy and robustness of 360-degree perceptual IQA. Our approach combines diverse patch sampling strategies with an advanced embedding-based refinement process, effectively addressing limitations observed in datasets like OIQA, CVIQ, and MVAQD. By integrating projection-based, latitude-based, and visual trajectory-based sampling techniques, our method provides a comprehensive solution that better captures the diverse perceptual experiences of 360-degree images, ensuring a more representative and detailed evaluation.

The embedding similarity refinement step further enhances patch selection by prioritizing the most informative patches, reducing redundancy, and aligning with the learning objectives. Extensive experiments on benchmark datasets demonstrated the effectiveness of this approach, with significant improvements in both accuracy and robustness. Notably, our framework achieved a performance gain of up to 4.5% in accuracy by selecting 40% to 50% of training samples while

discarding the less informative ones. This adaptive selection capability allows for more efficient training and reduces the impact of noisy samples, leading to improved performance of CNN-based 360-degree IQA models.

Overall, this work presents a robust and adaptive patch selection framework that not only enhances model training and prediction but also sheds light on the interactions between various sampling methods and their practical implications. The advancements proposed here offer a promising direction for future research in perceptual IQA, paving the way for more accurate and reliable assessments of 360-degree image quality.

## REFERENCES

- [1] A. Martin, Z. Emin, O. Cagri, and V. Giuseppe, "Introduction to immersive video technologies," in *Immersive Video Technologies*. Academic Press, 2023, pp. 3–24.
- [2] M. R. Intellect, "360-degree camera market poised for significant expansion: Projected to grow from usd 3.2 billion in 2024 to usd 6.8 billion by 2031," 2024, accessed: 2024-09-24. [Online]. Available: <https://shorturl.at/M8vZV>
- [3] A. Perkis, C. Timmerer, S. Baraković, J. Husić, and *et al.*, "Qualinet white paper on definitions of immersive media experience (imex)," *ENQEMSS, 14th QUALINET meeting (online)*, 2020.
- [4] M. Huang, Q. Shen, A. Ma, A. Bovik, P. Gupta, R. Zhou, and X. Cao, "Modeling the perceptual quality of immersive images rendered on head mounted displays: Resolution and compression," *IEEE TIP*, vol. 27, no. 12, pp. 6039–6050, 2018.
- [5] Y. Liu, X. Yin, Y. Wang, Z. Yin, and Z. Zheng, "HVS-based perception-driven no-reference omnidirectional image quality assessment," *IEEE TIM*, vol. 72, pp. 1–11, 2022.
- [6] M. Zhou, L. Chen, X. Wei, X. Liao, Q. Mao, H. Wang, H. Pu, J. Luo, T. Xiang, and B. Fang, "Perception-oriented u-shaped transformer network for 360-degree no-reference image quality assessment," *IEEE TB*, vol. 69, no. 2, pp. 396–405, 2023.
- [7] C. Zhang and S. Liu, "No-reference omnidirectional image quality assessment based on joint network," in *30th ACM ICM*, 2022, pp. 943–951.
- [8] L. Yang, M. Xu, T. Liu, L. Huo, and X. Gao, "TVFormer: Trajectory-guided visual quality assessment on 360° images with transformers," in *30th ACM ICM*, 2022, pp. 799–808.
- [9] J. Li, Y. Zhao, W. Ye, K. Yu, and S. Ge, "Attentive deep stitching and quality assessment for 360° omnidirectional images," *IEEE JSTSP*, vol. 14, no. 1, pp. 209–221, 2020.
- [10] C. Tian, F. Shao, X. Chai, Q. Jiang, L. Xu, and Y.-S. Ho, "Viewport-sphere-branch network for blind quality assessment of stitched 360° omnidirectional images," *IEEE TCSVT*, vol. 33, no. 6, pp. 2546–2560, 2023.
- [11] A. Sendjasi, M. Larabi, and S. Benkabou, "Adaptive patch labeling and multi-label feature selection for 360-degree image quality assessment," in *IEEE MMSP*, Poitiers, France, 2023, pp. 1–6.
- [12] Y. Sun, A. Lu, and L. Yu, "Weighted-to-spherically-uniform quality evaluation for omnidirectional video," *IEEE Signal Processing Letters*, vol. 24, pp. 1408–1412, 2017.
- [13] S. Chen, Y. Zhang, Y. Li, Z. Chen, and Z. Wang, "Spherical structural similarity index for objective omnidirectional video quality assessment," in *IEEE ICME*, San Diego, CA, USA, 2018, pp. 1–6.
- [14] Y. LeCun, Y. Bengio, and G. Hinton, "Deep learning," *nature*, vol. 521, no. 7553, pp. 436–444, 2015.
- [15] E. Charniak, *Introduction au deep learning*. Dunod, 2021.
- [16] C. Li, M. Xu, L. Jiang, S. Zhang, and X. Tao, "Viewport proposal cnn for 360° video quality assessment," in *IEEE CVPR*, pp. 10 169–10 178.
- [17] W. Sun, X. Min, G. Zhai, K. Gu, H. Duan, and S. Ma, "MC360IQA: A multi-channel CNN for blind 360-degree image quality assessment," in *IEEE JSTSP*, vol. 14, no. 1, 2020, pp. 64–77.
- [18] J. Xu, W. Zhou, and Z. Chen, "Blind omnidirectional image quality assessment with viewport oriented graph convolutional networks," *IEEE TCSVT*, vol. 31, no. 5, pp. 1724–1737, 2021.
- [19] A. Sendjasi and M. Larabi, "Attention-aware patch-based cnn for blind 360-degree image quality assessment," *Sensors*, vol. 23, no. 21, 2023.
- [20] L. Yang, M. Xu, X. Deng, and B. Feng, "Spatial attention-based non-reference perceptual quality prediction network for omnidirectional images," in *IEEE ICME*, Shenzhen, China, 2021, pp. 1–6.
- [21] C. Li, M. Xu, X. Du, and Z. Wang, "Bridge the gap between vqa and human behavior on omnidirectional video: A large-scale dataset and a deep learning model," in *26th ACM ICM*, 2018, pp. 932–940.
- [22] H. Kim, H. Lim, and Y. Ro, "Deep virtual reality image quality assessment with human perception guider for omnidirectional image," *IEEE TCSVT*, vol. 30, no. 4, pp. 917–928, 2020.
- [23] H. Jiang, G. Jiang, M. Yu, Y. Zhang, Y. Yang, Z. Peng, F. Chen, and Q. Zhang, "Cubemap-based perception-driven blind quality assessment for 360-degree images," *IEEE TIP*, vol. 30, pp. 2364–2377, 2021.
- [24] S. García, J. Luengo, and F. Herrera, *Data preprocessing in data mining*. Springer, 2015, vol. 72.
- [25] A. Sendjasi, M. Larabi, and F. Cheikh, "Perceptually-weighted CNN for 360-degree image quality assessment using visual scan-path and JND," in *IEEE ICIP*, Anchorage, AK, USA, 2021, pp. 1439–1443.
- [26] Y. Fan and C. Chen, "Omniqnet: Multiscale feature aggregation convolutional neural network for omnidirectional image assessment," *Applied Intelligence*, pp. 1–17, 2024.
- [27] Y. Zhou, Y. Sun, L. Li, K. Gu, and Y. Fang, "Omnidirectional image quality assessment by distortion discrimination assisted multi-stream network," *IEEE TCSVT*, pp. 1–1, 2021.
- [28] L. Liu, P. Ma, C. Wang, and D. Xu, "Omnidirectional image quality assessment with knowledge distillation," *IEEE SPL*, vol. 30, pp. 1562–1566, 2023.
- [29] A. Sendjasi, M. Larabi, and F. Cheikh, "Convolutional neural networks for omnidirectional image quality assessment: A benchmark," *IEEE TCSVT*, vol. 32, no. 11, pp. 7301–7316, 2022.
- [30] A. Dosovitskiy, L. Beyer, and A. K. *et al.*, "An image is worth 16x16 words: Transformers for image recognition at scale," in *ICLR*, 2021. [Online]. Available: <https://openreview.net/forum?id=YicbFdNTTy>
- [31] N. Tofghand, E. Hedi, N. Imamoglu, C. Ozcinar, E. Erdem, and A. Erdem, "ST360IQ: No-reference omnidirectional image quality assessment with spherical vision transformers," in *IEEE ICASSP*, Rhodes Island, Greece, 2023, pp. 1–5.
- [32] D. Liu, L. Zhang, L. Wan, Y. Yao, J. Ma, and Y. Zhang, "Dual-level blind omnidirectional image quality assessment network based on human visual perception," *IACSA*, vol. 14, no. 9, 2023.
- [33] T. Wu, S. Shi, H. Cai, M. Cao, J. Xiao, Y. Zheng, and Y. Yang, "Assessor360: Multi-sequence network for blind omnidirectional image quality assessment," in *Advances in Neural Information Processing Systems*, vol. 36. Curran Associates, Inc., 2023, pp. 64957–64970.
- [34] K. He, X. Zhang, S. Ren, and J. Sun, "Deep residual learning for image recognition," in *IEEE CVPR*, Las Vegas, NV, USA, 2016, pp. 770–778.
- [35] L. Kuncheva, A. Arnaiz, F. Díez-Pastor, and A. Gunn, "Instance selection improves geometric mean accuracy: a study on imbalanced data classification," *Progress in Artificial Intelligence*, vol. 8, pp. 215–228, 2019.
- [36] W. Chen, Y. Liu, W. Wang, E. Bakker, T. Georgiou, P. Fieguth, L. Liu, and M. Lew, "Deep learning for instance retrieval: A survey," *IEEE TPAMI*, vol. 45, no. 6, pp. 7270–7292, 2022.
- [37] D. Noton and L. Stark, "Scanpaths in saccadic eye movements while viewing and recognizing patterns," *Vision research*, vol. 11, no. 9, pp. 929–IN8, 1971.
- [38] D. Martin, A. Serrano, A. Bergman, G. Wetzstein, and B. Masia, "Scan360: A generative model of realistic scanpaths for 360° images," *IEEE TVCG*, vol. 28, no. 5, pp. 2003–2013, 2022.
- [39] A. Sendjasi and M. Larabi, "Self patch labeling using quality distribution estimation for cnn-based 360-iqa training," in *IEEE ICIP*, 2023, pp. 2640–2644.
- [40] Z. Zhao, L. Wang, H. Liu, and J. Ye, "On similarity preserving feature selection," *IEEE TKDE*, vol. 25, no. 3, pp. 619–632, 2013.
- [41] P. Mahalanobis, "On the generalized distance in statistics," *Proc. of the Nation. Acad. Sci.,(India)*, vol. 2, pp. 49–5, 1936.
- [42] C. Bishop and N. Nasrabadi, *Pattern recognition and machine learning*. Springer, 2006, vol. 4, no. 4.
- [43] Y. She and A. Owen, "Outlier detection using nonconvex penalized regression," *Journal of the American Statistical Association*, vol. 106, no. 494, pp. 626–639, 2011.
- [44] F. Nie, H. Huang, X. Cai, and C. Ding, "Efficient and robust feature selection via joint  $\ell_{2,1}$ -norms minimization," in *NIPS*. Vancouver, Canada: Curran Associates Inc., 2010, p. 1813–1821.
- [45] ITU-R, *Methodology for the subjective assessment of the quality of television pictures BT Series Broadcasting service*, 2012, vol. 13.